Feasibility Study of Single-crystal Si Islands Manufacturing by Microscale Printing of Nanoparticles and Laser Crystallization

Wan Shou, †,l Brandon Ludwig, †,l Letian Wang, ‡ Xiangtao Gong, † Xiaowei Yu, † Costas Grigoropoulos, ‡ Heng Pan*, †

[†]Department of Mechanical and Aerospace Engineering, Missouri University of Science and Technology, Rolla, 65409, USA

[‡]Laser Thermal Laboratory, Department of Mechanical Engineering, University of California, Berkeley, California, 94720-1740, USA

*Corresponding author: Heng Pan, hp5c7@mst.edu

ABSTRACT

Non-vacuum printing of single crystals would be ideal for high performance functional devices (such as electronics) fabrication, yet challenging for most materials, especially, for inorganic semiconductors. Currently, the printed films are dominantly in amorphous, polycrystalline or nanoparticle films. In this article, manufacturing of single-crystal silicon micro/nano island is attempted. Different from traditional vapor deposition for silicon thin film preparation, silicon nanoparticle ink was aerosol printed followed by confined laser melting and crystallization allowing potential fabrication of single-crystal silicon micro/nano islands. It is also shown asfabricated Si islands can be transfer printed onto polymer substrates for potential application of flexible electronics. The additive nature of this technique suggests a scalable and economical approach for high crystallinity semiconductor printing.

KEYWORDS

Aerosol printing, laser crystallization, confinement, silicon nanoparticle ink, flexible electronics

Direct printing, as a large area and low-cost fabrication technology, has received increasing interest and become essential for the development of flexible/stretchable electronics ¹⁻⁴, microelectronics⁵⁻⁶. Various emerging conductive materials and (such metal nanoparticles/nanowires⁷⁻¹⁰, carbon nanotube¹¹⁻¹³, graphene^{14,15}) and semiconductors (both organic¹⁶⁻¹⁸ and inorganic¹⁹⁻²²) have been printed for electronic components. Among various applications, single-crystals are highly desired for high performance device fabrication due to their high mobility²³. Recently, printing single-crystal organic semiconductor²⁴⁻²⁷ and organicinorganic hybrid perovskites^{28,29} have been demonstrated. However, higher performance inorganic semiconductor (such as Si and Ge) has not been realized to be printed into singlecrystal directly. Indirectly, single-crystal nanowires have been fabricated and transfer printed³⁰⁻³², although controlling location and orientation of nanowire array in a large area is subtle. By now, inorganic single-crystal semiconductor device fabrication mainly relies on lithographic processing^{33,34}, and vacuum based vapor-liquid-solid growth approaches^{35,36}. Thus, non-vacuum, scalable, inexpensive process for single-crystal semiconductors manufacturing is highly desired.

Currently, single-crystal Si is still the most widely used semiconductor in electronic and optoelectronic applications, such as high-performance transistors^{37,38}, photovoltaics^{39,40} and photodetector⁴¹, etc. However, its manufacturing largely relies on Czochralski (Cz) growth method⁴². Non-vacuum crystallization of amorphous Si (a-Si) thin film is considered as an alternative paradigm to fabricate high quality crystalline Si⁴³. Various energy sources have been utilized to crystallize amorphous Si thin film, including pulsed and continuous wave (CW) lasers^{37,44-50}, electron beam⁵¹, and strip heater⁵². In order to directly crystallize a-Si film to single-crystal on amorphous substrates, such as SiO₂, it would be preferred that all the materials are melted to exclude any pre-existed nucleus⁵³; thereby, lead to a scenario where crystal growth

from limited nucleation sites (ideally one nucleation site), which maximizes the crystalline grain size⁵⁴. Typically, sizes of the islands are several tens of μm in length and width, and <1 μm in thickness. Such sizes are sufficiently large for preparation of many devices and sufficient small to ensure single crystalline growth of the islands. Gibbons⁵⁵ shows 20 µm×2 µm Si islands on amorphous substrate can be laser recrystallized with formation of single-crystalline stripes. Nanoscale single-crystal fabrication^{44,56,57} has been demonstrated recently in confined domains on amorphous substrates both theoretically⁵⁸ and experimentally^{53,56,59}. It is suggested that the size of single crystal should be correlated with the sizes of laser beams as well as the pulse duration (scanning speed) used for recrystallization in order to increase the probability of forming single crystal⁵⁸. From previous literatures, three typical confining configurations are used: (1) Using pre-patterning techniques to confine the Si within a well-defined domain^{49,60}, rather than a whole film; (2) confining Si within a capillary^{41,61} or isolating Si as a nanopillar^{53,56,59}; and (3) embedding or capping Si with silicon oxide layer^{62,63}, which also depress the dewetting⁶⁴⁻⁶⁷. Generally, confinement provides an effective way to prevent heat dissipation, modulate cooling rate and prevent dewetting of melted thin films. However, a straightforward and reusable confining method is needed to simplify the process and lower the cost. Besides, most of these studies rely on vacuum-based chemical/physical vapor deposition (CVD/PVD) or electron beam evaporation (EBE) to prepare the thin film, which inevitably increases the processing and equipment costs. Among various approaches, laser crystallization is an excellent candidate due to its versatility such as vacuum-free/maskless nature, area-selective rapid processing, and scalability to large-area manufacturing. The crystallization method for large area processing can be combined with a direct printing approach for Si film preparation, which is becoming significant for low cost manufacturing of high performance devices⁶⁸⁻⁷².

Here, we reported a potential manufacturing scheme for printing single-crystal Si islands in ambient environment. An industrial viable microscale printing approach, i.e. aerosol printing, is used to print silicon nanoparticle (NP) patterns on wafer scales. Subsequently, a quartz slide was employed to densify, planarize and confine the printed Si nanoparticle films. A CW laser was irradiated through the transparent quartz piece onto the printed Si nanoparticles, where can be heated, melted and crystallized. The laser melted liquid stripe could break into separated islands, whose size, spacing and morphology can be dictated by laser scan speed and confining gaps (the packing density of the nanoparticles). The isolated domains are in microscale range which contain limited number of nucleation sites facilitating single crystal formation. The confining surface (e.g. fused quartz) is removed after laser crystallization. To prevent or reduce the attachment of crystalized structures on quartz, the substrate (e.g. nitride) exhibiting higher adhesion with Si compared with quartz could be used. The entire process circumvents expensive equipment (such as CVD or PVD, and photolithography), while maintaining high quality of crystallized Si, which paves the way toward low-cost high-performance device fabrication.

RESULTS AND DISCUSSION

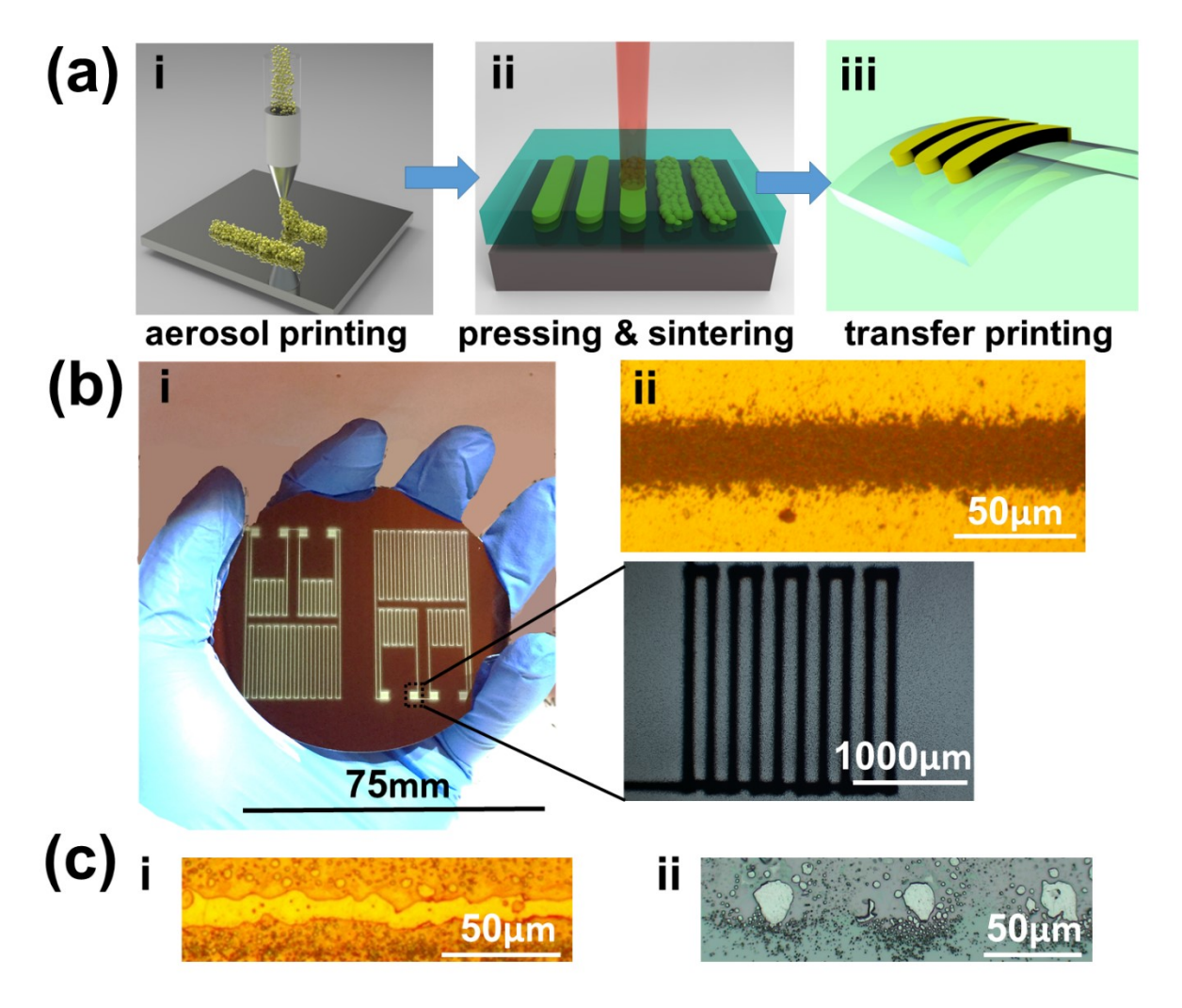


Figure 1. (a) Conceptual design of laser direct writing of crystalline nano-ribbon using confinement. i. Aerosol printing of microscale pattern using Si NPs; ii. Pressing and confined laser crystallization; iii. Transfer print of fabricated Si to flexible substrate. (b) Representative photographs and microscope images of printed Si pattern. i. Wafer scale printing; ii. The smallest continuous line by aerosol printing (c) Representative microscope images of i. laser processed continuous line; ii. laser processed Si islands after Secco etching.

Figure 1 (a) illustrates the Si ribbon/islands printing process that can be integrated with flexible substrates. Si patterns were firstly prepared by aerosol printing on Si substrates with 2 μm oxide or nitride films. The aerosol printing generates linewidth down to ~20 μm, as shown in Fig.1b-ii. Printed linewidth is mainly controlled by adjusting printing speed (1-5mm/s, details in Fig. S2). The Si ink preparation and printing process are described in Methods. A photograph of

printed Si patterns on wafer scales is displayed in Figure 1(b)-i, which was printed within minutes. The printed Si patterns exhibiting high porosity and rough surfaces were then pressed and planarized using a transparent quartz slide (fused quartz, details can be found in Materials and Methods), as indicated in Figure 1(a)-ii. To ensure uniform pressing and confinement over a large area, air cushion pressing used in nanoimprinting process is utilized⁷³. An inflatable airbag was incorporated in the system with pressure supplied and regulated by a gas cylinder. The details of the pressing system are described in supplementary materials (Fig. S3). CW laser irradiates through the quartz slide on the planarized and confined Si patterns to induce melting and recrystallization (as illustrated in Figure 1(a)-ii). Representative crystallized Si line and islands were displayed in Figure 1(c). After disassembling, the crystallized Si can be peeled off (Figure S4) and transferred to the target polymer substrates (Figure 1(a)-iii).

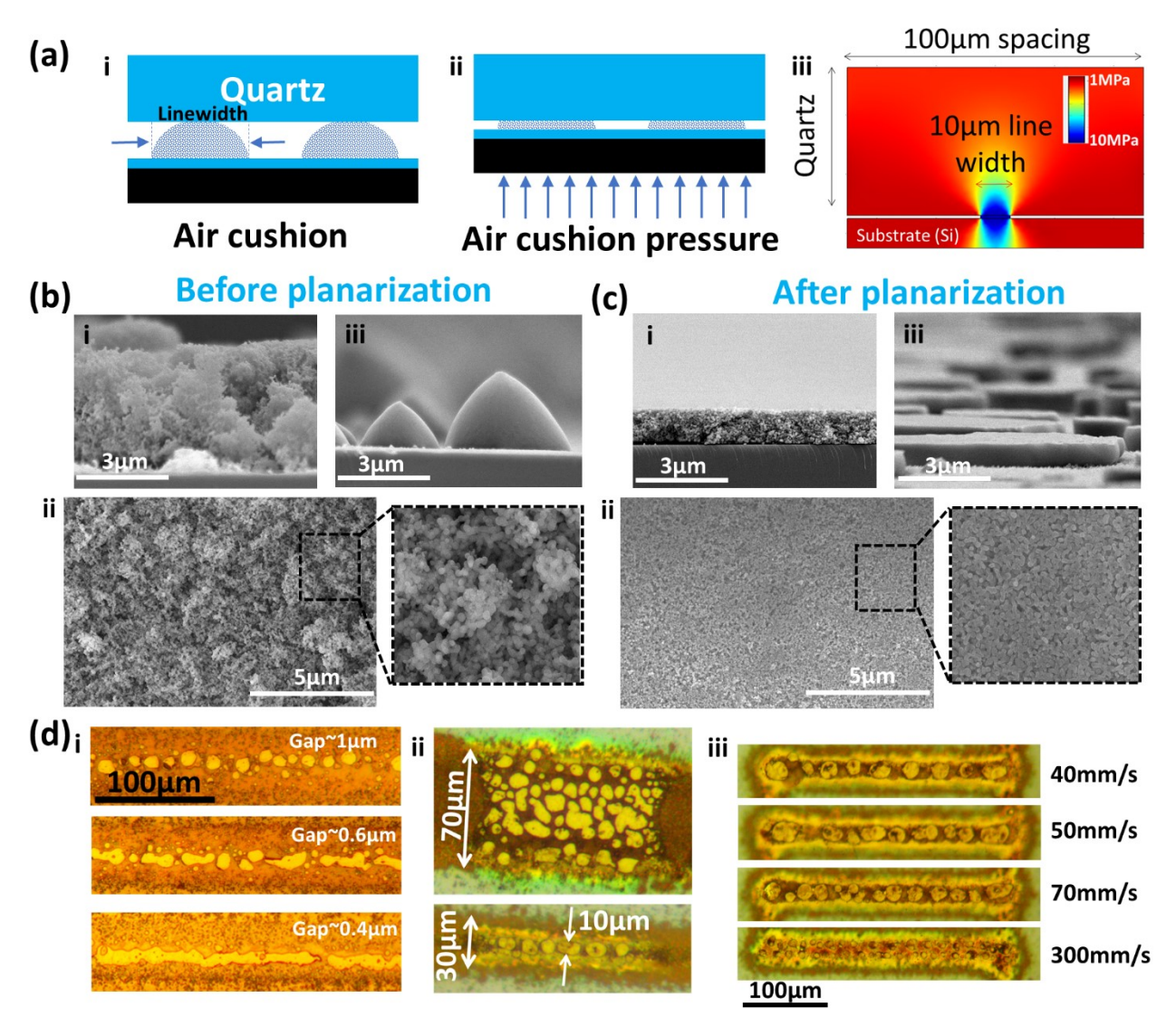


Figure 2. The influence of pressing-assisted confining on laser melting and crystallization of Si nanoparticles. (a) Schematic of pressing and corresponding FEM simulation. (b) Printed Si nanoparticle without pressing (i) Cross-section SEM image of the as printed Si NPs. (ii) Top view SEM image of the printed Si NPs (low and high magnifications) (iii) Si dewets after laser processing without confinement. (c) Printed Si nanoparticle after pressing (i) Cross-section SEM image of the pressed Si NPs. (ii) Top view SEM image of the pressed Si NPs (low and high magnifications) (iii) Flat Si domains after laser processing with confinement. (d) Optical images of Si NPs processed with different parameters: (i) confining gap, (ii) printed linewidth, and (iii) laser scanning speed.

Pressure up to 2.5 MPa has been reported⁷³ for nanoimprinting by air cushion. Finite element method (FEM) simulation (**Figure 2**a) shows that with 1 MPa air cushion pressure, the

pressure applied on aerosol printed lines can reach 10 MPa (assuming 100 μm line spacing and 10 μm linewidth). It is reported that nanopowders can be dry pressed and cold-welded to green density (>62%) by 50 MPa uniaxial pressure γ4-76. Thus, it is estimated that nanoparticle packing density reaches ≥50% with ~1 MPa air cushion pressing. The pressure in the range of 0.68-0.83 MPa are used in current study. Planarization and densification of printed nanoparticles can be clearly observed in the scanning electron microscope (SEM) cross-sectional view of nanoparticles before and after pressing. Figure 2 (b-i&ii) shows the as-printed morphology, where Si nanoparticles are loosely deposited within the printed area, exhibiting high non-evenness and porosity, with averaged thickness of about 5 μm. After pressing (Figure 2c-i&ii), the nanoparticles become closely packed with thickness ~400 nm to 1 μm. A clear reduction of porosity/thickness and significant improvement of flatness and uniformity are shown from the above comparison.

Laser is focused and scanned along the length direction of printed ribbons (Figure 1a-ii) to induce melting and crystallization. Without the quartz confinement, the melted Si droplets dewet the SiO₂/Si substrate and form islands with contact angle in the range ~73° to 100° (Figure 2b-iii). With the confinement, disk-shaped islands with contact angle of ~80-90° were formed (Figure 2d-iii). The confining quartz largely suppresses the dewetting. Furthermore, it is noticed that melted ribbons break up into separated islands, with the size, spacing and morphology of the islands dictated by pressing pressure, laser scan speed and substrate surface properties. By increasing the pressure, the spacing between islands gradually decreases until a continuous line was formed. A clear transition from "discrete islands (break-up)" into "continuous line (no break-up)" can be observed (Figure 2d-i) when the confining gap decreases from ~1 μm to sub-500 nm. Besides the gap, it is found that the smaller the linewidth is, the more likely islands line

up along the printed trace (Figure 2d-ii) and form a linear array of islands. This indicates the location and spacing of islands can be controlled by aerosol printing parameters (length and width of the printed trace). Figure 2d-iii shows that laser scanning speed alters the size and spacing of the islands. It is found increasing laser scanning speed reduces the size of island and the spacing between islands. Slower scanning speed provides longer melt duration allowing more time for melted nanoparticles to coalescence and form large islands. In this study it is found the scanning speed in 50-70 mm/s and power 25-35 W can fully melt the ribbons and produce large islands. It is also found the islands tend to form elongated shapes on nitride surface, while on oxide surface round shaped islands are mostly found (Fig.S5). The difference in island/ribbon morphology is mainly due to lower contact angle of liquid Si on nitride surface compared with that on oxide surface.

To shed lights onto the confinement effect on break-up process that determines the island size, the stability criteria of liquid thin film is re-visited. It is known for a thin, continuous and confined liquid on a substrate, the stability (no break-up) condition is when the contact angle between the liquid and bounding surface is < 90° 77-79. The contact angle of liquid Si on SiO₂/Si substrate as observed in Figure 2b-iii satisfies this condition. However, break-up is commonly observed in current study. Recent Lattice Boltzmann Model shows the balling effect in selective laser melting (SLM) are strongly influenced by local powder arrangement^{80,81}. It is then believed that the break-up condition in melted NP ribbons would critically depend on perturbation and porosity introduced by random particle packing. NP planarization reduces the perturbation and porosity which suppresses the break-up of melted NP films as observed in Figure 2(d) and Figure 3(a-d). To understand the effect of particle packing density on break-up process, Computational Fluid Dynamics (CFD) simulation of the evolution of liquid NP film bounded by two surfaces

were performed (details in supplementary materials, Fig.S6). The simulation results suggest that higher packing density effectively suppresses or delays break-up process and vice versa as observed in Figure 2d-i.

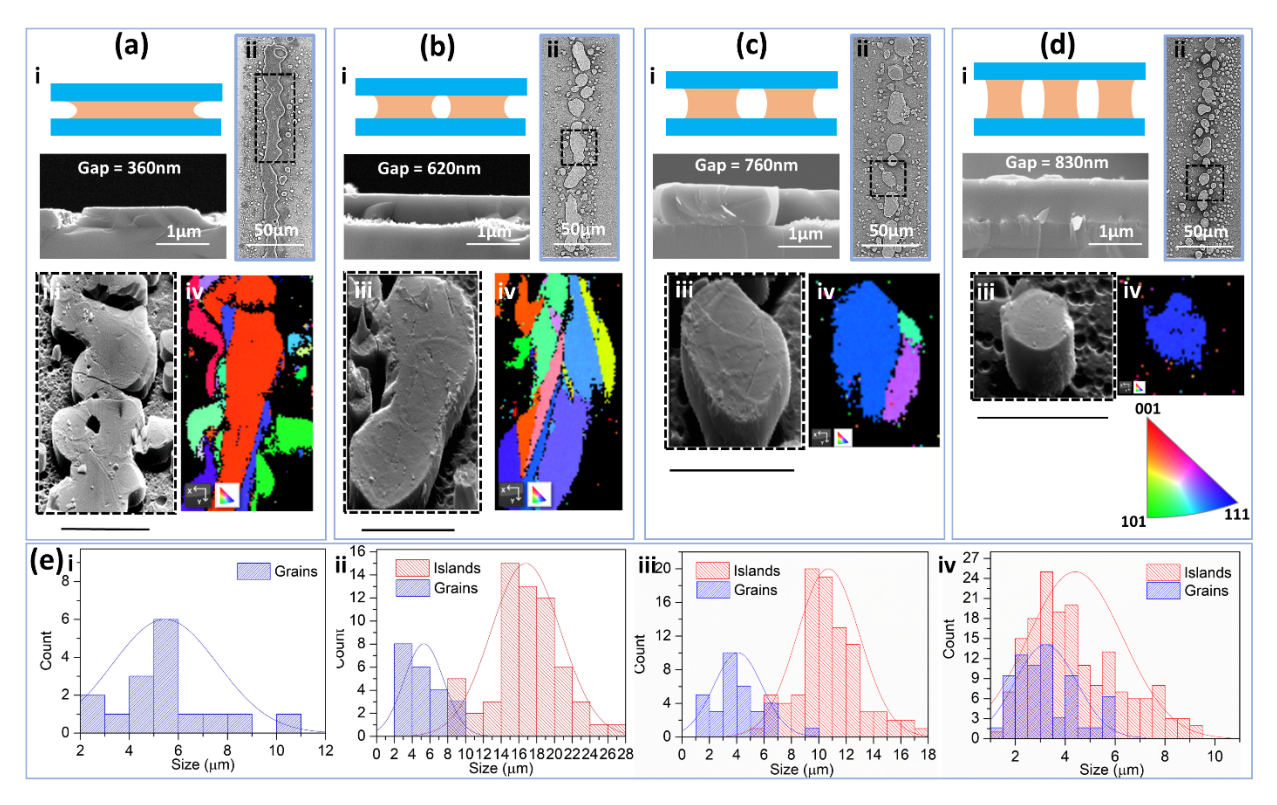


Figure 3. Influence of confining gap on the morphology and crystalline structure of annealed Si. (a) Mode I, continuous long ribbon. (b) Mode II, elongated islands. (c) Mode III, isolated islands. (d) Mode IV, single-crystal islands. (i) Schematic draw of melted Si under confinement and annealed Si thickness; (ii) SEM image of annealed Si; SEM image of zoomed in Si pattern with gran boundary revealed by Secco etching (iii) and corresponding EBSD map (iv). Scale bar for iii & iv through (a) to (d) are $10~\mu m$. (e) The distribution of grain size and islands size for four different modes.

Based on this finding, the confining gap was varied to modulate the spacing and size of islands with laser scanning speed fixed at 70 mm/s. Figure 3 (a-d) shows the SEM morphology (i&ii) and crystallinity (ii&iv) of the laser crystallized Si islands subjected to various confining gaps, as indicated by the SEM measured film thickness. To examine the crystallinity of these ribbons/islands, the Secco etchant was used to reveal the grain boundary in the sample^{49,82} and

then characterized with SEM. With the smallest gap (360 nm), the break-up was largely suppressed and a continuous long ribbon was obtained (length $\geq 100 \, \mu \text{m}$, width $\sim 10 \, \mu \text{m}$). Grain boundaries are clearly seen indicating a polycrystal structure. Increasing the gap to 620 nm leads to elongated islands (length ~20 μm, width ~10 μm) that are isolated with no obvious grain boundaries. Further increasing of the gap left clearly isolated islands (length ~10 μm, width ~10 μm), which were dominated by a large grain and some small defects on the edges. At even larger gap, the large grain almost occupied the entire domain (~5 µm×5 µm) indicating the formation of single-crystal islands. The crystallinity of these islands were further confirmed via electron backscattering diffraction (EBSD) mapping, showing good consistance with the Secco etching results. Statistical analysis of grain size (as measured from EBSD) are presented along with the distribution of island size in Figure 3(e) for each confining gap. It is found with small gap, the grain size are largely less than island size while with large gap, grain size starts to overlap with island size indicating formation of single-crystal islands. Namely, island size can be tuned to accommodate only one grain, leading to the fabrication of single-crystal island. Further, no obvious impurity was detected through energy-dispersive X-ray spectroscopy (EDX) in laser crystallized islands (Fig. S6). Therefore, by tuning the confining gap with air cushion pressure, Si nanoparticles can be melted and crystallized into single-crystal islands of certain sizes.

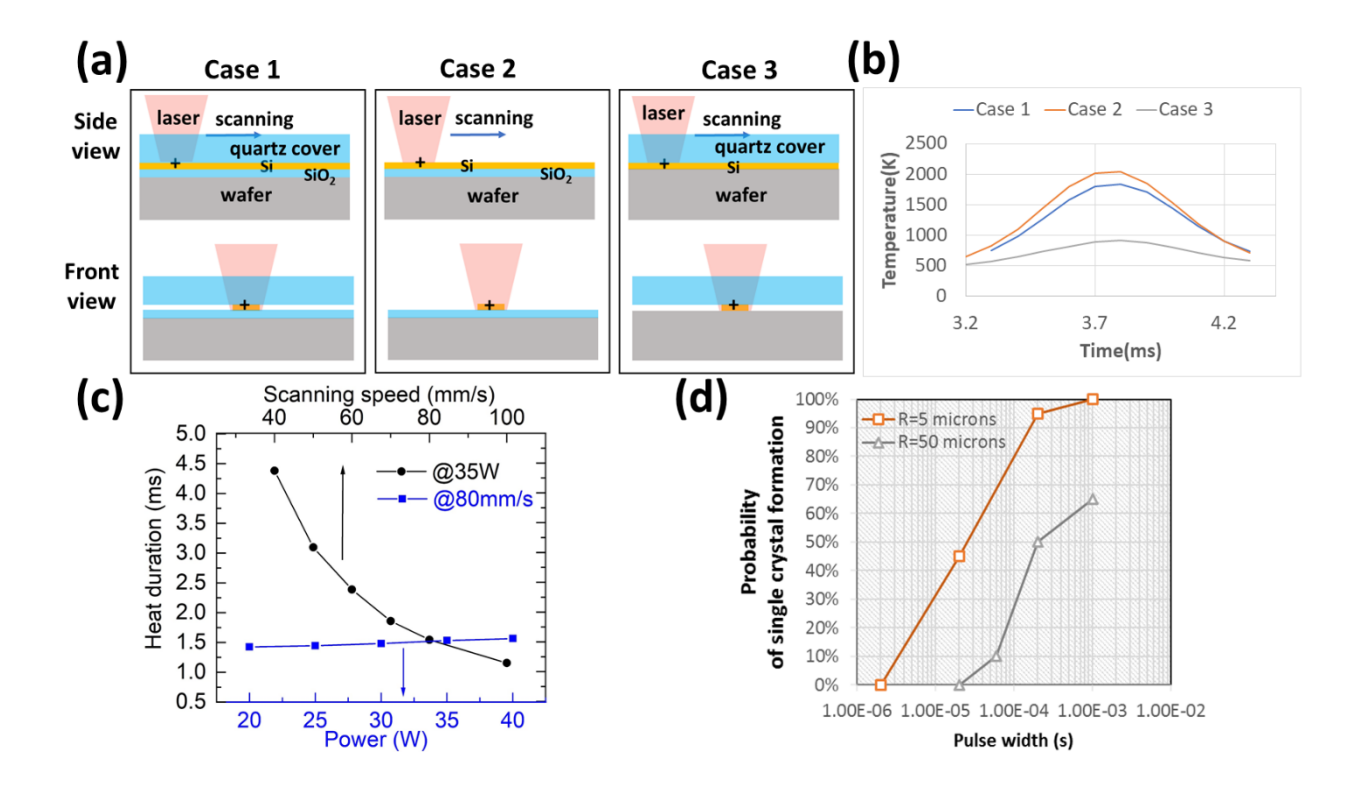


Figure 4. Simulations of CW laser scanning induced melting and crystallization of printed strip. (a) Schematics of simulation configuration ("+" indicates the temperature probe location). (b) Temperature evolution measured at the probe location for three cases: 1. with quartz cover and with SiO₂ on the surface (experimental setup). 2. without quartz cover and with SiO₂ on the surface. 3. with quartz cover and without SiO₂ on the surface. (c) Laser heating duration at different laser powers and scanning speeds for case 1 (experimental setup). (d) Modeling results on probability of single crystal formation obtained with various laser pulse width in various domain sizes.

To investigate the laser-induced melting and crystallization of Si NPs in the present study, we combined the macroscale heat transfer model with nanoscale nucleation and crystal growth model⁵⁸. Firstly, numerical simulations were conducted to estimate the temperature history in a laser scanning configuration as presented in **Figure 4a**. Laser heating was modeled as a moving heat source on Si stripe on substrate. The boundary conditions and the material properties details of thermal model are provided in supplementary materials. Temperature evolution was probed at the top of the stripe. With laser scanning speed of 80 mm/s and laser power of 35 W, the heating

duration is ~1-2 ms with peak temperature increased by introducing a 2 μm thermal oxide layer (as shown in Figure 4b, Case 1 and 3). In most cases, the peak temperature could not reach the melting point if the substrate is bare silicon (with native oxide) without thick oxide layer. Lowthermal-conductivity oxide can make the heat energy accumulated within the silicon stripe comparing to bare silicon substrate. Potentially, the heat duration can be controlled by the thickness of oxide layer. The quartz cover is another potential tool to modify the heat duration. The numerical simulations (Figure 4c) show that with the increase of laser power or decrease of scanning speed, the heat duration increases in the range of 1 to several milliseconds. The heat duration is more dependent on the scanning speed than the laser power. The estimated cooling rates are on the order of 10⁵-10⁶ K/s. Secondly, a nucleation/crystallization model coupled with laser heating and surrounding medium cooling was invoked. Laser heating was approximated by a Gaussian shaped pulsed heating with 1 ms pulse width (in the range of estimated heat duration from previous heat transfer simulation). Critical parameters used in modeling (chemical potential $\Delta\mu$, melting temperature T_m , surface properties) were taken from Molecular Dynamics using Tersoff potential⁵⁴ (details of the crystallization model in supplementary materials). Various domain size and laser duration were modeled and the probability of forming single crystal was plotted in Figure 4d. The modeling results show longer laser pulses greatly increase of the probability of forming single crystals. For domain size at R=50 µm, it is unlikely to obtain 100% single crystals even with ~ms laser pulse width. For smaller domain size at R=5 μm, using millisecond laser pulses generally yields single crystals. Since the laser scanning scheme adopted in present work generates heating profiles similar to ms laser pulse heating (Figure 4c), the simulation supports experimental results that several-micron-sized single-crystal islands can be fabricated using the laser scanning approach.

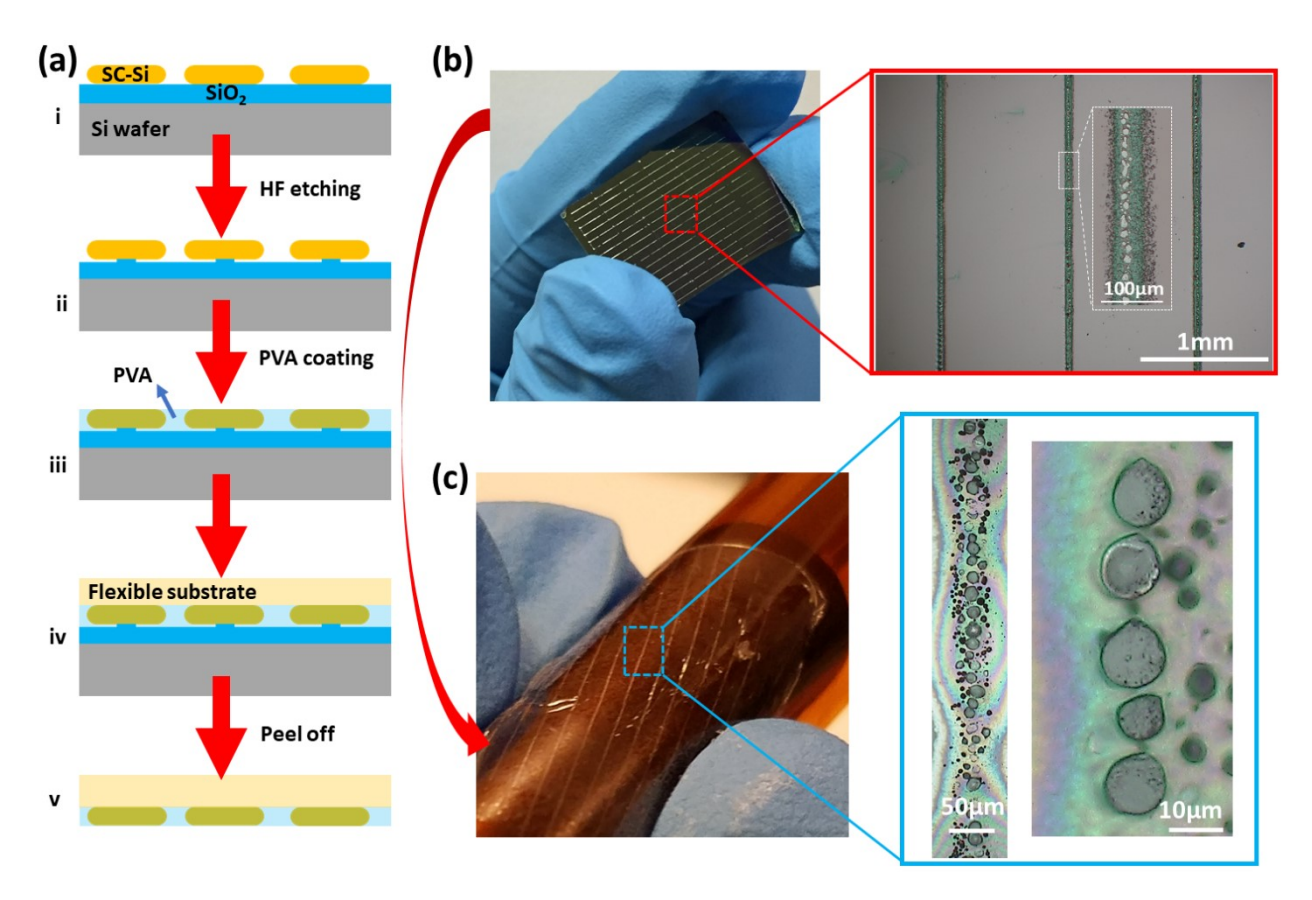


Figure 5. Transfer of fabricated Si islands. (a) Schematic of detailed transfer procedure. i. As fabricated Si on wafer with 2 µm thermal oxide layer; ii. Under-cut making using HF etching; iii. Coating of adhesive PVA layer; iv. Flexible substrate attachment; v. Peel off with Si islands on flexible substrate. Photography and optical image of fabricated Si islands (b) before and (c) after transfer on flexible substrate.

Finally, attempts were made to transfer print as-fabricated islands onto flexible substrates. Heterogeneous integration of high-performance semiconductor materials with flexible/polymer substrates represents a key step towards realizing high-performance integrated electronics. Transfer printing has been largely employed for integration of pre-fabricated microstructured silicon ribbons, single-crystal ribbons, and nanowire devices^{30-34,84} onto flexible platform. However, these devices were dominantly fabricated by IC micro-machining and subtractive methods on silicon-on-insulator (SOI) or bulk wafers. Current work suggests an additive and direct printing approach to generate pre-patterned Si islands for transfer printing. The transfer

printing process is illustrated in Figure 5(a). Firstly, as-fabricated Si islands (on 2 μm oxide) were etched using 5% HF to make under-cut. Then, the sample was thoroughly cleaned with DI water and dried with nitrogen gas flow. Subsequently, the sample was dried in Ar at 350°C for 30 min to make the SiO₂ hydrophobic (allowing detachment of Polyvinyl alcohol (PVA) from SiO₂/Si substrate during peeling off step). Then PVA solution was coated as adhesive film on the sample to be transferred. Receiving substrates (Polyimide) was pressed gently on top of the PVA allowing fully contact of PVA films with receiving substrate. By peeling off the receiving substrate, the Si islands were transferred to the receiving substrate. Figure 5 shows linear array of Si islands after laser crystallization (Figure 5b) and after being transferred to a plastic substrate (Figure 5c). The successful transferring process of Si can be potentially used for fabricating flexible thin-film transistor (TFT) arrays after fabrication of electrodes^{30-32,84-86}.

CONCLUSIONS

In summary, we have demonstrated a potential additive scheme to fabricate single-crystal Si structures via aerosol printing, planarization and confined laser crystallization. Here, aerosol printing offers a mask-free, high-efficiency approach for direct Si patterning at microscales. The confining (and pressing) system significantly planarizes and densifies the printed Si patterns. Millisecond laser crystallization of the confined Si nanoparticles leads to the formation of single-crystal islands of ~5µm wide and <1µm thick. Furthermore, the as-fabricated Si islands were successfully transferred onto flexible substrates.

MATERIALS AND METHODS

Si ink: Different from previous Si printing^{21,22}, binder-free Si ink was developed here. The Si nanopowders have an average size of 30 nm, which is provided by Advanced Chemicals Supplier (purity of >99.99%). Silicon nanopowders were mixed with methanol and ethanol in

weight ratio of 1:9:90. Typically, 0.4 g of Si nanopowders, 3.6 g of methanol, and 36 g of ethanol were used. After mixing, the solution was sonicated for 10 min twice with a 10 min gap before printing.

Other materials: Quartz slide was purchased from Ted Pella, which is made from high purity fused quartz (with a nominal softening point of 1683°C). Silicon wafer with 2 µm thermal oxide or nitride was provided by University Wafer. A customized inflatable airbag was bought from MatJack Inc. to planarize the Si nanoparticles with uniform pressure. More details can be found in supplementary materials.

Laser Parameters: A single mode ytterbium fiber laser (IPG, 1065 nm, CW, 100 W) was directed into a galvanometer for high speed (up to 800 mm s⁻¹) laser sintering. A defocused laser spot with diameter of ~80 μm was selected to cover the whole printed Si line. Typically, sintering was conducted with laser power of ~35 W and scanning speed of 70 mm/s. The laser crystallization is performed with an in-situ pressing/planarization system (details in supplementary materials).

Characterization: SEM images and EDX analysis were taken in Hitachi S-4700 or Helios Nanolab 600. EBSD mapping were conducted in Helios Nanolab 600.

Secco etching: Mixture of HF (48%) and K₂Cr₂O₇ solution (44 g K₂Cr₂O₇ dissolved in 1 L of H₂O, or 0.15 M) in a ratio of 2:1 were prepared as the original etchant. One part of the original etchant was freshly diluted with 4 parts of distilled water to etch the crystallized Si sample. A typical moderate etching time of 45 seconds was used⁸².

Heat Transfer Simulation

To understand the temperature evolution during CW laser crystallization, a basic heat conduction finite element analysis (FEA) model was developed to predict the temperature history. The

simulation dimensions are 600 μm×600 μm×200 μm for the wafer and quartz cover, and 600

μm×50 μm×0.8 μm for the printed Si line. For the wafer with oxide, 2 μm SiO₂ was used to

replace the top 2 µm of the wafer. More details about the modeling can be found in

supplementary materials.

ASSOCIATED CONTENT

Supporting Information.

All the following figures are formatted in one PDF file as supporting information. Supporting

Information is available free of charge on the Internet at http://pubs.acs.org.

Fig. S1. TEM and XRD of Si nanoparticles.

Fig. S2. The influence of printing speed on printed linewidth.

Fig. S3. Schematics of confined laser processing setup.

Fig. S4. The workflow of confined laser melting, crystallization and transfer printing.

Fig. S5. Ribbon morphology on different substrates.

Fig. S6. Simulation scheme to study break-up of melted nanoparticles in confined configuration.

Fig. S7. EDX analysis of representative sintered Si islands.

Fig. S8. Simulation domain dimensions and boundary conditions.

Fig. S9. Modeling liquid crystallization in confined domains.

AUTHOR INFORMATION

Corresponding Author

*Email: hp5c7@mst.edu

17

Author Contributions

¹These authors contributed equally.

The authors declare no competing financial interest.

ACKNOWLEDGMENTS

The work is supported by the collaborative NSF Grant CMMI-1363392 and 1363313 to C.G. and H.P., and NSF Grant CMMI-1635256. This research was also partially supported Intelligent System Center (ISC) and Material Research Center (MRC) at Missouri University of Science and Technology and ORAU Ralph E. Powe Junior Faculty Enhancement Award. Their financial supports are greatly appreciated.

REFERENCES

- (1) Rogers, J. A.; Someya, T.; Huang, Y. Materials and Mechanics for Stretchable Electronics. *Science* **2010**, *327*, 1603-1607.
- (2) Yin, Z.; Huang, Y.; Bu, N.; Wang, X.; Xiong, Y. Inkjet Printing for Flexible Electronics: Materials, Processes and Equipments. *Chinese Sci. Bull.* **2010**, *55*, 3383–3407.
- (3) Yu, X.; Mahajan, K. B.; Shou, W.; Pan, H. Materials, Mechanics, and Patterning Techniques for Elastomer-Based Stretchable Conductors. *Micromachines* **2017**, 8, 7
- (4) Mohammed, M. G.; Kramer, R. All-Printed Flexible and Stretchable Electronics. *Adv. Mater.* **2017**, *29*, 1604965.
- (5) Rim, Y. S.; Bae, S.-H.; Chen, H.; De Marco, N.; Yang, Y. Recent Progress in Materials and Devices toward Printable and Flexible Sensors. *Adv. Mater.* **2016**, *28*, 4415–4440.
- (6) Yu, X.; Shou, W.; Mahajan, B. K.; Huang, X.; Pan, H. Materials, Processes, and Facile Manufacturing for Bioresorbable Electronics: A Review. *Adv. Mater.* **2018**, *30*, 1707624.
- (7) Ko, S. H.; Pan, H.; Grigoropoulos, C. P.; Luscombe, C. K.; Fréchet, J. M. J.; Poulikakos, D. All-Inkjet-Printed Flexible Electronics Fabrication on a Polymer Substrate by Low-Temperature High-Resolution Selective Laser Sintering of Metal Nanoparticles. *Nanotechnology* **2007**, *18*, 345202.

- (8) Ko, S. H.; Pan, H.; Grigoropoulos, C. P.; Luscombe, C. K.; Fréchet, J. M. J.; Poulikakos, D. Air Stable High Resolution Organic Transistors by Selective Laser Sintering of Ink-Jet Printed Metal Nanoparticles. *Appl. Phys. Lett.* **2007**, *90*, 141103.
- (9) Ko, S. H.; Chung, J.; Pan, H.; Grigoropoulos, C. P.; Poulikakos, D. Fabrication of Multilayer Passive and Active Electric Components on Polymer Using Inkjet Printing and Low Temperature Laser Processing. *Sensors Actuators A Phys.* **2007**, *134*, 161–168.
- (10) Bade, S. G. R.; Li, J.; Shan, X.; Ling, Y.; Tian, Y.; Dilbeck, T.; Besara, T.; Geske, T.; Gao, H.; Ma, B. Fully Printed Halide Perovskite Light-Emitting Diodes with Silver Nanowire Electrodes. *ACS Nano* **2015**, *10*, 1795–1801.
- (11) Kordás, K.; Mustonen, T.; Tóth, G.; Jantunen, H.; Lajunen, M.; Soldano, C.; Talapatra, S.; Kar, S.; Vajtai, R.; Ajayan, P. M. Inkjet Printing of Electrically Conductive Patterns of Carbon Nanotubes. *Small* **2006**, *2*, 1021–1025.
- (12) Small, W. R.; in het Panhuis, M. Inkjet Printing of Transparent, Electrically Conducting Single-walled Carbon-nanotube Composites. *Small* **2007**, *3*, 1500–1503.
- (13) Okimoto, H.; Takenobu, T.; Yanagi, K.; Miyata, Y.; Shimotani, H.; Kataura, H.; Iwasa, Y. Tunable Carbon Nanotube Thin-Film Transistors Produced Exclusively via Inkjet Printing. *Adv. Mater.* **2010**, *22*, 3981–3986.
- (14) Torrisi, F.; Hasan, T.; Wu, W.; Sun, Z.; Lombardo, A.; Kulmala, T. S.; Hsieh, G.-W.; Jung, S.; Bonaccorso, F.; Paul, P. J. Inkjet-Printed Graphene Electronics. *ACS Nano* **2012**, *6*, 2992–3006.
- (15) Li, Y.; Gao, T.; Yang, Z.; Chen, C.; Luo, W.; Song, J.; Hitz, E.; Jia, C.; Zhou, Y.; Liu, B. 3D-Printed, All-in-One Evaporator for High-Efficiency Solar Steam Generation under 1 Sun Illumination. *Adv. Mater.* **2017**, *29*, 1700981.
- (16) Garnier, F.; Hajlaoui, R.; Yassar, A.; Srivastava, P. All-Polymer Field-Effect Transistor Realized by Printing Techniques. *Science* **1994**, *265*, 1684–1686.
- (17) Li, J.; Zhao, Y.; Tan, H. S.; Guo, Y.; Di, C.-A.; Yu, G.; Liu, Y.; Lin, M.; Lim, S. H.; Zhou, Y. A Stable Solution-Processed Polymer Semiconductor with Record High-Mobility for Printed Transistors. *Sci. Rep.* **2012**, *2*, 754.
- (18) Minari, T.; Kanehara, Y.; Liu, C.; Sakamoto, K.; Yasuda, T.; Yaguchi, A.; Tsukada, S.; Kashizaki, K.; Kanehara, M. Room-Temperature Printing of Organic Thin-Film Transistors with π-Junction Gold Nanoparticles. *Adv. Funct. Mater.* **2014**, *24*, 4886–4892.
- (19) Ridley, B. A.; Nivi, B.; Jacobson, J. M. All-Inorganic Field Effect Transistors Fabricated by Printing. *Science* **1999**, *286*, 746–749.
- (20) Shimoda, T.; Matsuki, Y.; Furusawa, M.; Aoki, T.; Yudasaka, I.; Tanaka, H.; Iwasawa, H.; Wang, D.; Miyasaka, M.; Takeuchi, Y. Solution-Processed Silicon Films and Transistors. *Nature* **2006**, *440* (7085), 783.

- (21) Härting, M.; Zhang, J.; Gamota, D. R.; Britton, D. T. Fully Printed Silicon Field Effect Transistors. *Appl. Phys. Lett.* **2009**, *94*, 193509.
- (22) Sani, N.; Robertsson, M.; Cooper, P.; Wang, X.; Svensson, M.; Ersman, P. A.; Norberg, P.; Nilsson, M.; Nilsson, D.; Liu, X. All-Printed Diode Operating at 1.6 GHz. *Proc. Natl. Acad. Sci.* **2014**, *111*, 11943–11948.
- (23) Takeya, J.; Yamagishi, M.; Tominari, Y.; Hirahara, R.; Nakazawa, Y.; Nishikawa, T.; Kawase, T.; Shimoda, T.; Ogawa, S. Very High-Mobility Organic Single-Crystal Transistors with in-Crystal Conduction Channels. *Appl. Phys. Lett.* **2007**, *90*, 102120.
- (24) Minemawari, H.; Yamada, T.; Matsui, H.; Tsutsumi, J.; Haas, S.; Chiba, R.; Kumai, R.; Hasegawa, T. Inkjet Printing of Single-Crystal Films. *Nature* **2011**, *475*, 364.
- (25) Kim, Y.; Yoo, B.; Anthony, J. E.; Park, S. K. Controlled Deposition of a High-performance Small-molecule Organic Single-crystal Transistor Array by Direct Ink-jet Printing. *Adv. Mater.* **2012**, *24*, 497–502.
- (26) Park, K. S.; Cho, B.; Baek, J.; Hwang, J. K.; Lee, H.; Sung, M. M. Single-Crystal Organic Nanowire Electronics by Direct Printing from Molecular Solutions. *Adv. Funct. Mater.* **2013**, *23*, 4776–4784.
- (27) Rigas, G.-P.; Payne, M. M.; Anthony, J. E.; Horton, P. N.; Castro, F. A.; Shkunov, M. Spray Printing of Organic Semiconducting Single Crystals. *Nat. Commun.* **2016**, *7*, 13531.
- (28) Lee, L.; Baek, J.; Park, K. S.; Lee, Y.-E.; Shrestha, N. K.; Sung, M. M. Wafer-Scale Single-Crystal Perovskite Patterned Thin Films Based on Geometrically-Confined Lateral Crystal Growth. *Nat. Commun.* **2017**, *8*, 15882.
- (29) Gu, Z.; Wang, K.; Li, H.; Gao, M.; Li, L.; Kuang, M.; Zhao, Y. S.; Li, M.; Song, Y. Direct-Writing Multifunctional Perovskite Single Crystal Arrays by Inkjet Printing. *small* **2017**, *13*, 1603217.
- (30) Menard, E.; Nuzzo, R. G.; Rogers, J. A. Bendable Single Crystal Silicon Thin Film Transistors Formed by Printing on Plastic Substrates. *Appl. Phys. Lett.* **2005**, *86*, 93507.
- (31) Ahn, J.-H.; Kim, H.-S.; Lee, K. J.; Jeon, S.; Kang, S. J.; Sun, Y.; Nuzzo, R. G.; Rogers, J. A. Heterogeneous Three-Dimensional Electronics by Use of Printed Semiconductor Nanomaterials. *Science* **2006**, *314*, 1754–1757.
- (32) Meitl, M. A.; Zhu, Z.-T.; Kumar, V.; Lee, K. J.; Feng, X.; Huang, Y. Y.; Adesida, I.; Nuzzo, R. G.; Rogers, J. A. Transfer Printing by Kinetic Control of Adhesion to an Elastomeric Stamp. *Nat. Mater.* **2006**, *5*, 33.
- (33) Khang, D.-Y.; Jiang, H.; Huang, Y.; Rogers, J. A. A Stretchable Form of Single-Crystal Silicon for High-Performance Electronics on Rubber Substrates. *Science* **2006**, *311*, 208–212.

- (34) Baca, A. J.; Meitl, M. A.; Ko, H. C.; Mack, S.; Kim, H.; Dong, J.; Ferreira, P. M.; Rogers, J. A. Printable Single-crystal Silicon Micro/nanoscale Ribbons, Platelets and Bars Generated from Bulk Wafers. *Adv. Funct. Mater.* **2007**, *17*, 3051–3062.
- (35) Wagner, R. S.; Ellis, W. C. Vapor-liquid-solid Mechanism of Single Crystal Growth. *Appl. Phys. Lett.* **1964**, *4*, 89–90.
- (36) Chen, K.; Kapadia, R.; Harker, A.; Desai, S.; Kang, J. S.; Chuang, S.; Tosun, M.; Sutter-Fella, C. M.; Tsang, M.; Zeng, Y. Direct Growth of Single-Crystalline III–V Semiconductors on Amorphous Substrates. *Nat. Commun.* **2016**, *7*, 10502.
- (37) Im, J. S.; Sposili, R. S.; Crowder, M. A. Single-Crystal Si Films for Thin-Film Transistor Devices. *Appl. Phys. Lett.* **1997**, *70*, 3434–3436.
- (38) Yuan, H.-C.; Ma, Z.; Roberts, M. M.; Savage, D. E.; Lagally, M. G. High-Speed Strained-Single-Crystal-Silicon Thin-Film Transistors on Flexible Polymers. *J. Appl. Phys.* **2006**, *100*, 13708.
- (39) Zhao, J.; Wang, A.; Green, M. A.; Ferrazza, F. 19.8% Efficient "honeycomb" Textured Multicrystalline and 24.4% Monocrystalline Silicon Solar Cells. *Appl. Phys. Lett.* **1998**, *73*, 1991–1993.
- (40) Yoshikawa, K.; Kawasaki, H.; Yoshida, W.; Irie, T.; Konishi, K.; Nakano, K.; Uto, T.; Adachi, D.; Kanematsu, M.; Uzu, H. Silicon Heterojunction Solar Cell with Interdigitated Back Contacts for a Photoconversion Efficiency over 26%. *Nat. Energy* **2017**, *2*, 17032.
- (41) Ji, X.; Lei, S.; Yu, S.-Y.; Cheng, H. Y.; Liu, W.; Poilvert, N.; Xiong, Y.; Dabo, I.; Mohney, S. E.; Badding, J. V. Single-Crystal Silicon Optical Fiber by Direct Laser Crystallization. *ACS Photonics* **2016**, *4*, 85–92.
- (42) Evers, J.; Klüfers, P.; Staudigl, R.; Stallhofer, P. Czochralski's Creative Mistake: A Milestone on the Way to the Gigabit Era. *Angew. Chemie Int. Ed.* **2003**, *42*, 5684–5698.
- (43) Im, J. S.; Kim, H. J.; Thompson, M. O. Phase Transformation Mechanisms Involved in Excimer Laser Crystallization of Amorphous Silicon Films. *Appl. Phys. Lett.* **1993**, *63*, 1969–1971.
- (44) Chimmalgi, A.; Hwang, D. J.; Grigoropoulos, C. P. Nanoscale Rapid Melting and Crystallization of Semiconductor Thin Films. *Nano Lett.* **2005**, *5*, 1924–1930.
- (45) Taheri, M. L.; McGowan, S.; Nikolova, L.; Evans, J. E.; Teslich, N.; Lu, J. P.; LaGrange, T.; Rosei, F.; Siwick, B. J.; Browning, N. D. In Situ Laser Crystallization of Amorphous Silicon: Controlled Nanosecond Studies in the Dynamic Transmission Electron Microscope. *Appl. Phys. Lett.* **2010**, *97*, 32102.
- (46) Saboundji, A.; Mohammed-Brahim, T.; Andrä, G.; Bergmann, J.; Falk, F. Thin Film Transistors on Large Single Crystalline Regions of Silicon Induced by CW Laser Crystallization. *J. Non. Cryst. Solids* **2004**, *338*, 758–761.

- (47) Andrä, G.; Bergmann, J.; Falk, F. Laser Crystallized Multicrystalline Silicon Thin Films on Glass. *Thin Solid Films* **2005**, *487*, 77–80.
- (48) Michaud, J. F.; Rogel, R.; Mohammed-Brahim, T.; Sarret, M. CW Argon Laser Crystallization of Silicon Films: Structural Properties. *J. Non. Cryst. Solids* **2006**, *352*, 998–1002.
- (49) Park, S. J.; Ku, Y. M.; Kim, K. H.; Kim, E. H.; Choo, B. K.; Choi, J. S.; Kang, S. H.; Lim, Y. J.; Jang, J. CW Laser Crystallization of Amorphous Silicon; Dependence of Amorphous Silicon Thickness and Pattern Width on the Grain Size. *Thin Solid Films* **2006**, *511*, 243–247.
- (50) Said-Bacar, Z.; Prathap, P.; Cayron, C.; Mermet, F.; Leroy, Y.; Antoni, F.; Slaoui, A.; Fogarassy, E. CW Laser Induced Crystallization of Thin Amorphous Silicon Films Deposited by EBE and PECVD. *Appl. Surf. Sci.* **2012**, *258*, 9359–9365.
- (51) Amkreutz, D.; Müller, J.; Schmidt, M.; Hänel, T.; Schulze, T. F. Electron-beam Crystallized Large Grained Silicon Solar Cell on Glass Substrate. *Prog. Photovoltaics Res. Appl.* **2011**, *19*, 937–945.
- (52) Sameshima, T.; Kaneko, Y.; Andoh, N. Rapid Joule Heating of Metal Films Used to Crystallize Silicon Films. *Appl. Phys. A* **2002**, *74*, 719–723.
- (53) In, J. Bin; Xiang, B.; Hwang, D. J.; Ryu, S.-G.; Kim, E.; Yoo, J.-H.; Dubon, O.; Minor, A. M.; Grigoropoulos, C. P. Generation of Single-Crystalline Domain in Nano-Scale Silicon Pillars by near-Field Short Pulsed Laser. *Appl. Phys. A* **2014**, *114*, 277–285.
- (54) Shou, W.; Pan, H. Silicon-Wall Interfacial Free Energy via Thermodynamics Integration. *J. Chem. Phys.* **2016**, *145*, 184702.
- (55) Gibbons, J. F.; Lee, K. F.; Magee, T. J.; Peng, J.; Ormond, R. CW Laser Recrystallization Of< 100> Si on Amorphous Substrates. *Appl. Phys. Lett.* **1979**, *34*, 831–833.
- (56) Xiang, B.; Hwang, D. J.; In, J. Bin; Ryu, S.-G.; Yoo, J.-H.; Dubon, O.; Minor, A. M.; Grigoropoulos, C. P. In Situ TEM near-Field Optical Probing of Nanoscale Silicon Crystallization. *Nano Lett.* **2012**, *12*, 2524–2529.
- (57) Wang, L.; Rho, Y.; Shou, W.; Hong, S.; Kato, K.; Eliceiri, M.; Shi, M.; Grigoropoulos, C. P.; Pan, H.; Carraro, C. Programming Nanoparticles in Multiscale: Optically Modulated Assembly and Phase Switching of Silicon Nanoparticle Array. *ACS Nano* **2018**, *12*, 2231–2241.
- (58) Pan, H.; Shou, W. Single Crystal Formation in Micro/nano-Confined Domains by Melt-Mediated Crystallization without Seeds. *J. Phys. D. Appl. Phys.* **2015**, *48*, 225302.
- (59) Liu, Y.; Deal, M. D.; Saraswat, K. C.; Plummer, J. D. Single-Crystalline Si on Insulator in Confined Structures Fabricated by Two-Step Metal-Induced Crystallization of Amorphous Si. *Appl. Phys. Lett.* **2002**, *81*, 4634–4636.
- (60) Hara, A.; Yoshino, K.; Takeuchi, F.; Sasaki, N. Selective Single-Crystalline-Silicon Growth at the Pre-Defined Active Region of a Thin Film Transistor on Glass by Using Continuous Wave Laser Irradiation. *Jpn. J. Appl. Phys.* **2003**, *42*, 23.

- (61) Arora, H.; Du, P.; Tan, K. W.; Hyun, J. K.; Grazul, J.; Xin, H. L.; Muller, D. A.; Thompson, M. O.; Wiesner, U. Block Copolymer Self-Assembly–directed Single-Crystal Homo-and Heteroepitaxial Nanostructures. *Science* **2010**, *330*, 214–219.
- (62) Kim, D. K.; Jeong, W. H.; Bae, J. H.; Hwang, T. H.; Roh, N. S.; Kim, H. J. Selective Area Crystallization of Amorphous Silicon Using Micro-Patterned SiO₂ Capping Layer. *J. Cryst. Growth* **2010**, *312*, 2335–2338.
- (63) Schade, M.; Mchedlidze, T.; Kittler, M.; Leipner, H. S. Light Induced Crystallization of an Amorphous Silicon Film Embedded between Silicon Oxide Layers. *Phys. status solidi* **2014**, *251*, 439–445.
- (64) Danielson, D. T.; Sparacin, D. K.; Michel, J.; Kimerling, L. C. Surface-Energy-Driven Dewetting Theory of Silicon-on-Insulator Agglomeration. *J. Appl. Phys.* **2006**, *100*, 83507.
- (65) Cheynis, F.; Bussmann, E.; Leroy, F.; Passanante, T.; Müller, P. Dewetting Dynamics of Silicon-on-Insulator Thin Films. *Phys. Rev. B* **2011**, *84*, 245439.
- (66) Bussmann, E.; Cheynis, F.; Leroy, F.; Müller, P.; Pierre-Louis, O. Dynamics of Solid Thin-Film Dewetting in the Silicon-on-Insulator System. *New J. Phys.* **2011**, *13*, 43017.
- (67) Aouassa, M.; Favre, L.; Ronda, A.; Maaref, H.; Berbezier, I. The Kinetics of Dewetting Ultra-Thin Si Layers from Silicon Dioxide. *New J. Phys.* **2012**, *14*, 63038.
- (68) Grigoropoulos, C. P. *Transport in Laser Microfabrication: Fundamentals and Applications*; Cambridge University Press, 2009.
- (69) Son, Y.; Yeo, J.; Moon, H.; Lim, T. W.; Hong, S.; Nam, K. H.; Yoo, S.; Grigoropoulos, C. P.; Yang, D.-Y.; Ko, S. H. Nanoscale Electronics: Digital Fabrication by Direct Femtosecond Laser Processing of Metal Nanoparticles. *Adv. Mater.* **2011**, *23*, 0935–9648.
- (70) Hong, S.; Yeo, J.; Kim, G.; Kim, D.; Lee, H.; Kwon, J.; Lee, H.; Lee, P.; Ko, S. H. Nonvacuum, Maskless Fabrication of a Flexible Metal Grid Transparent Conductor by Low-Temperature Selective Laser Sintering of Nanoparticle Ink. *ACS Nano* **2013**, *7*, 5024–5031.
- (71) Lee, D.; Paeng, D.; Park, H. K.; Grigoropoulos, C. P. Vacuum-Free, Maskless Patterning of Ni Electrodes by Laser Reductive Sintering of NiO Nanoparticle Ink and Its Application to Transparent Conductors. *ACS Nano* **2014**, *8*, 9807–9814.
- (72) Shou, W.; Mahajan, B. K.; Ludwig, B.; Yu, X.; Staggs, J.; Huang, X.; Pan, H. Low-Cost Manufacturing of Bioresorbable Conductors by Evaporation–Condensation-Mediated Laser Printing and Sintering of Zn Nanoparticles. *Adv. Mater.* **2017**, *29*, 0935–9648.
- (73) Gao, H.; Tan, H.; Zhang, W.; Morton, K.; Chou, S.Y. Air Cushion Press for Excellent Uniformity, High Yield, and Fast Nanoimprint Across a 100 mm Field. *Nano Lett.* **2006**, 6, 2438-2441.

- (74) Ewsuk, K.G.; Ellerby, D.T.; DiAntonio, C.B. Analysis of Nanocrystalline and Microcrystalline ZnO Sintering Using Master Sintering Curves. *J Am Ceram Soc.* **2006**, 89(6), 2003-2009.
- (75) Schwarz, S.; Thron, A.M.; Rufner, J.; van Benthem, K.; Guillon, O. Low Temperature Sintering of Nanocrystalline ZinC Oxide: Effect of Heating Rate Achieved by Field Assisted Sintering/Spark Plasma Sintering. *J Am Ceram Soc.* **2012**, 95(8), 2451-2457.
- (76) Heckel, R.W. Density-pressure relationships in powder compaction. *Trans Metall Soc AIME* **1961**, 221(4), 671-675.
- (77) Chen, H.; Amirfazli, A.; Tang, T. Modeling Liquid Bridge between Surfaces with Contact Angle Hysteresis. *Langmuir* **2013**, *29*, 3310–3319.
- (78) Luo, C.; Heng, X.; Xiang, M. Behavior of a Liquid Drop between Two Nonparallel Plates. *Langmuir* **2014**, *30*, 8373–8380.
- (79) Shi, Z.; Zhang, Y.; Liu, M.; Hanaor, D. A. H.; Gan, Y. Dynamic Contact Angle Hysteresis in Liquid Bridges. *Colloids Surfaces A Physicochem. Eng. Asp.* **2018**, *555*, 365–371.
- (80) Gusarov, A. V; Smurov, I. Modeling the Interaction of Laser Radiation with Powder Bed at Selective Laser Melting. *Phys. Procedia* **2010**, *5*, 381–394.
- (81) Körner, C.; Attar, E.; Heinl, P. Mesoscopic Simulation of Selective Beam Melting Processes. *J. Mater. Process. Technol.* **2011**, *211*, 978-987.
- (82) Zheng, C. Innovation in Photovoltaic Science, Engineering, and Policy: A Potential Trillion-Dollar Global Industry for Sustainable Energy. UC Berkeley 2014.
- (83) Falk, F.; Andrä, G. Laser Crystallization-a Way to Produce Crystalline Silicon Films on Glass or on Polymer Substrates. *J. Cryst. Growth* **2006**, *287*, 397–401.
- (84) Mack, S.; Meitl, M. A.; Baca, A. J.; Zhu, Z.-T.; Rogers, J. A. Mechanically Flexible Thin-Film Transistors That Use Ultrathin Ribbons of Silicon Derived from Bulk Wafers. *Appl. Phys. Lett.* **2006**, *88*, 213101.
- (85) Briseno, A. L.; Mannsfeld, S. C. B.; Ling, M. M.; Liu, S.; Tseng, R. J.; Reese, C.; Roberts, M. E.; Yang, Y.; Wudl, F.; Bao, Z. Patterning Organic Single-Crystal Transistor Arrays. *Nature* **2006**, *444*, 913.
- (86) Mannsfeld, S. C. B.; Sharei, A.; Liu, S.; Roberts, M. E.; McCulloch, I.; Heeney, M.; Bao, Z. Highly Efficient Patterning of Organic Single-Crystal Transistors from the Solution Phase. *Adv. Mater.* **2008**, *20*, 4044-4048.

TABLE OF CONTENT (TOC)

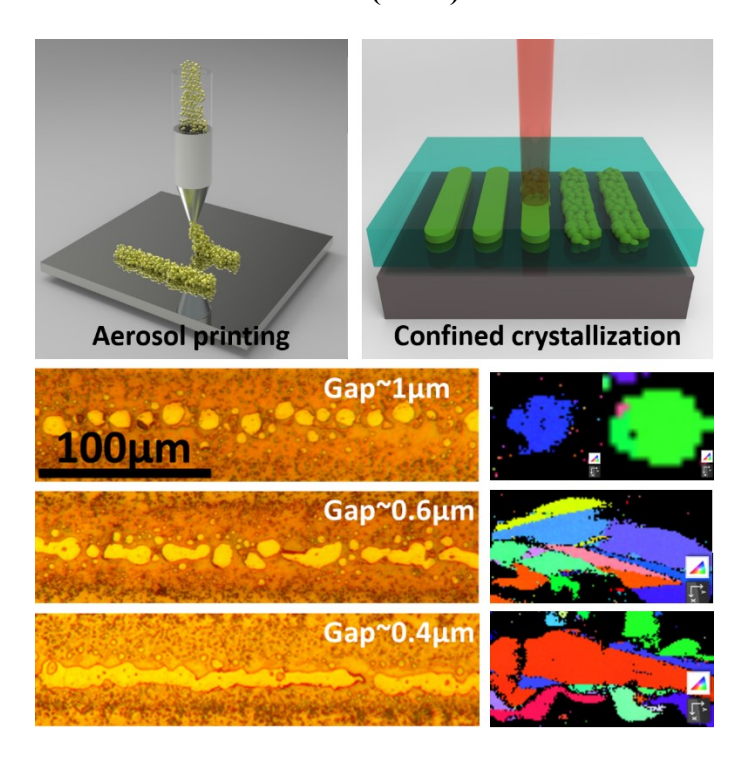


Figure Caption:

Figure 1. (a) Conceptual design of laser direct writing of crystalline nano-ribbon using confinement. i. Aerosol printing of microscale pattern using Si NPs; ii. Pressing and confined laser crystallization; iii. Transfer print of fabricated Si to flexible substrate. (b) Representative photographs and microscope images of printed Si pattern. i. Wafer scale printing; ii. The smallest continuous line by aerosol printing (c) Representative microscope images of i. laser processed continuous line; ii. laser processed Si islands after Secco etching.

Figure 2. The influence of pressing-assisted confining on laser melting and crystallization of Si nanoparticles. (a) Schematic of pressing and corresponding FEM simulation. (b) Printed Si nanoparticle without pressing (i) Cross-section SEM image of the as printed Si NPs. (ii) Top view SEM image of the printed Si NPs (low and high magnifications) (iii) Si dewets after laser processing without confinement. (c) Printed Si nanoparticle after pressing (i) Cross-section SEM image of the pressed Si NPs. (ii) Top view SEM image of the pressed Si NPs (low and high magnifications) (iii) Flat Si domains after laser processing with confinement. (d) Optical images of Si NPs processed with different parameters: (i) confining gap, (ii) printed linewidth, and (iii) laser scanning speed.

Figure 3. Influence of confining gap on the morphology and crystalline structure of annealed Si. (a) Mode I, continuous long ribbon. (b) Mode II, elongated islands. (c) Mode III, isolated islands. (d) Mode IV, single-crystal islands. (i) Schematic draw of melted Si under confinement and annealed Si thickness; (ii) SEM image of annealed Si; SEM image of zoomed in Si pattern with gran boundary revealed by Secco etching (iii) and corresponding EBSD map (iv). Scale bar for iii & iv through (a) to (d) are $10~\mu m$. (e) The distribution of grain size and islands size for four different modes.

Figure 4. Simulations of CW laser scanning induced melting and crystallization of printed strip. (a) Schematics of simulation configuration ("+" indicates the temperature probe location). (b) Temperature evolution measured at the probe location for three cases: 1. with quartz cover and with SiO₂ on the surface (experimental setup). 2. without quartz cover and with SiO₂ on the surface. 3. with quartz cover and without SiO₂ on the surface. (c) Laser heating duration at different laser powers and scanning speeds for case 1 (experimental setup). (d) Modeling results on probability of single crystal formation obtained with various laser pulse width in various domain sizes.

Figure 5. Transfer of fabricated Si islands. (a) Schematic of detailed transfer procedure. i. As fabricated Si on wafer with 2 µm thermal oxide layer; ii. Under-cut making using HF etching; iii. Coating of adhesive PVA layer; iv. Flexible substrate attachment; v. Peel off with Si islands on flexible substrate. Photography and optical image of fabricated Si islands (b) before and (c) after transfer on flexible substrate.